

Supplementary Material

A spatial and temporal risk assessment of the impacts of El Niño on the tropical forest carbon cycle: theoretical framework, scenarios and implications

Adriane Esquivel-Muelbert^{1,2*}, Amy C. Bennett^{1*}, Martin J. P. Sullivan¹, Jessica C. A. Baker³, Yoni Gavish¹, Michelle O. Johnson¹, Yunxia Wang¹, Alexander Chambers-Ostler¹, Marta Lisli Giannichi^{1,2}, Luciene Gomes¹, Michelle Kalamandeen¹, Kanhu Charan Pattnayak³ and Sophie Fauset^{4*}

¹ School of Geography, University of Leeds, Leeds, LS2 9JT, UK

² School of Geography, Earth and Environmental Sciences, University of Birmingham, Birmingham, B15 2TT, UK

³ School of Earth and Environment, University of Leeds, Leeds, LS2 9JT, UK

⁴ School of Geography, Earth and Environmental Science, University of Plymouth, Plymouth, PL4 8AA UK

S1-Methods for calculating climate variables

S2-Methods for calculating forest ignition potential

Figure S1 El Niño drivers, processes and impact

Figure S2 El Niño event in which grid-cells experienced maximum risk

Figure S3 Susceptibility and severity maps

Figure S4 Drivers of the risk score – severity vs susceptibility

Figure S5 Drivers of severity – T vs MCWD

Figure S6 Drivers of susceptibility – T vs MCWD vs ignition potential

Figure S7 Validation of risk metric

Appendix S1. Methods for Calculating Climate Variables

Temperature (T) data were taken from the Climatic Research Unit (CRU) TS4.01 gridded monthly product series [1]. These data are based on meteorological station data, interpolated to a $0.5^\circ \times 0.5^\circ$ global grid and available from 1901 to 2016 (Table 1). In addition, we used precipitation (P) from the Global Precipitation Climatology Centre (GPCC) V7 product, which is also based on station data and covers the period 1901–2013 [2].

In addition to these ground-based climate products, remote-sensing and reanalysis datasets were used. Such datasets can offer useful climate insights in regions where station density is low, such as over remote regions of tropical forest. We used the Tropical Rainfall Measuring Mission (TRMM) 3B43 V7 precipitation product, which combines satellite and gauge data to estimate precipitation from 1998 to 2016 [3]. Reanalysis 2-m T data were retrieved from the ERA-Interim Monthly Means of Daily Means product, which spans 1979 to 2016 and assimilates observational and model data [4].

Merging and Regridding

Precipitation from TRMM and temperature from ERA-Interim data were regridded to 0.5° spatial resolution, and then combined with GPCC and CRU data respectively, to form merged datasets of P and T. Regridding is the process of transforming data from its native grid (i.e., the source grid) to a target grid using interpolation. We used the Python package Iris (scitools.org.uk/iris/docs/latest/index.html) to regrid the TRMM and ERA-Interim data. With Iris it is possible to assign another climate dataset as the target grid, and thus it is straightforward to convert data from one grid to the grid of another dataset. We applied an area-weighted regridding scheme, whereby the value of each target grid cell is calculated as the mean of the source grid cells, weighted by their land surface area. This approach was used to ensure that all source grid points contributed to the regridded field, while accounting for the fact that grid cells differ in size with distance from the Equator.

To reduce computational time, data from GPCC, CRU, TRMM and ERA-Interim were clipped to the broadleaf tropical moist forest ecoregion [5] prior to merging the datasets. Linear relationships were calculated between GPCC and TRMM P, and between CRU and ERA-Interim T, using data from the periods of overlap (1998–2013 for P and 1979–2016 for T). The equations for the lines of best fit were used to linearly transform GPCC and CRU data to ensure consistency across the full range of the data, and to prevent artificial step changes at the point where datasets were merged.

$$CRU' = 1.093CRU - 2.576$$

$$GPCC' = 0.9899GPCC + 4.1360$$

Thus P (GPCC' and TRMM) and T (CRU' and ERA-Interim) are continuous from 1901 to 2016.

Cumulative Water Deficits

We used MCWD as an indicator of water stress [6]. MCWD is the maximum accumulated water deficit (WD) in each hydrological year for each grid cell. Monthly WD (mm month^{-1}) is defined as monthly P minus monthly ET, which was approximated at $100 \text{ mm month}^{-1}$ across all grid cells analysed [1]. For each grid cell the start of the hydrological cycle is defined as the mean wettest calendar month of the baseline period (1960 - 2016). If the wettest month of the year falls in the period January to May then the first hydrological cycle belongs to year y , if the wettest month falls in June or after then this hydrological year belongs to $y+1$ (i.e. the hydrological year is the year in which the dry season ends). This method allows us to account for shifts in the phase of the wet and dry seasons between the northern and southern hemispheres. For each hydrological year, cumulative water deficit is calculated by the following [6]:

$$\begin{aligned} & \text{if } WD_{n-1}(i, j) - ET_n(i, j) + P_n(i, j) < 0; \\ & \text{then } WD_n(i, j) = WD_{n-1}(i, j) - ET_n(i, j) + P_n(i, j) \end{aligned}$$

$$\text{else } WD_n(i, j) = 0$$

Calculating baselines and anomalies

For each grid cell across the tropical forest domain, the merged climate datasets were used to calculate baseline mean T and MCWD. Baselines, i.e. long-term averages, were calculated using data from 1960–2016 only, due to a decline in the number of meteorological stations prior to 1960.

Anomalies were calculated separately for El Niño 1982, El Niño 1997 and El Niño 2015. The start and end dates of each El Niño were identified using sea surface temperature (SST) anomalies over the Niño 3.4 region, with the El Niño period defined as the 12 months with the highest SST anomalies (May–April for all three El Niños). These 12 months were used to calculate either the mean-based (mean T from 1960–2016) or trend-based (mean T from 10-year period prior to the start of each El Niño) T anomalies for each El Niño. MCWD anomalies were calculated by taking the maximum accumulated water deficit of the 2 hydrological years beginning at the wettest month preceding the start of each El Niño period and subtracting either the mean-based (mean MCWD of the 1960-2016 hydrological years) or trend-based (mean MCWD of the 10 hydrological years prior to the start of each El Niño) baseline. The MCWD anomaly during the two-year window was used to describe the strongest moisture-stress suffered by each forest accounting for any temporal variation of the El Niño impact across the tropics.

Table S1. Climate products used to calculate the climate component of the risk score.

Variable	Product	Time span	Temporal resolution	Spatial resolution	Reference
Precipitation	Global Precipitation Climatology Centre (GPCC)	1901–2016	Monthly	0.5° × 0.5°	Schneider et al., 2016 [2]
	Tropical Rainfall Measuring Mission (TRMM) 3B43 V7	1997–2016	Monthly	0.25° × 0.25°	Huffman et al., 2007 [3]
Temperature	Climatic Research Unit (CRU)	1901–2016	Monthly	0.5° × 0.5°	Harris et al., 2014 [1]
	ERA-Interim Reanalysis	1979–2016	Monthly	0.25° × 0.25°	Dee et al., 2011 [4]

Appendix S2. Methods for calculating forest ignition potential

Extent of Forest Cover

We defined our area of interest based on the boundaries of the broadleaf tropical moist forest ecoregion [5]. To determine forest extent within the broadleaf tropical moist forest ecoregion, we used the 30-m resolution Global Forest Change (GFC) dataset [7], version 1.4 spanning 2000 to 2016 [earthenginepartners.appspot.com/science-2013-global-forest/download_v1.4.html]. Based on GFC tree cover dataset, we assessed the extent of forests in the years 2000 and 2014. For 2000, all pixels with tree cover above 30% were considered as forest. The extent of forest for 2014 was generated by subtracting forest losses and adding forest gains for 2000-2014 from the baseline 2000 forest extent. Tree cover in the GFC dataset was defined as canopy closure for all vegetation taller than 5m in height. Forest loss was defined as a stand-replacement disturbance or a change from forest to non-forest state, while forest gain was the inverse of the loss or a change from non-forest to forest. All processing was conducted in Google Earth Engine [code.earthengine.google.com].

Analysis of Forest Ignition Potential

To ensure compatibility with climate data, all calculations were performed within a 0.5 degree grid. We used forest edge as a proxy for forest ignition potential (I). Here, ignition potential was calculated as the percentage of forest within 1km from forest edge normalized by the total forest area within grid cell. There is no global ignition potential data readily available for El Niño 1982 and El Niño 1997. Thus, data from 2000, the first year available in the Global Forest Change dataset, was used to calculate fragmentation for El Niño 1982 and El Niño 1997, while fragmentation data from 2014 was used for El Niño 2015. The two forest cover maps from 2000 and 2014 were used in the ignition potential analysis.

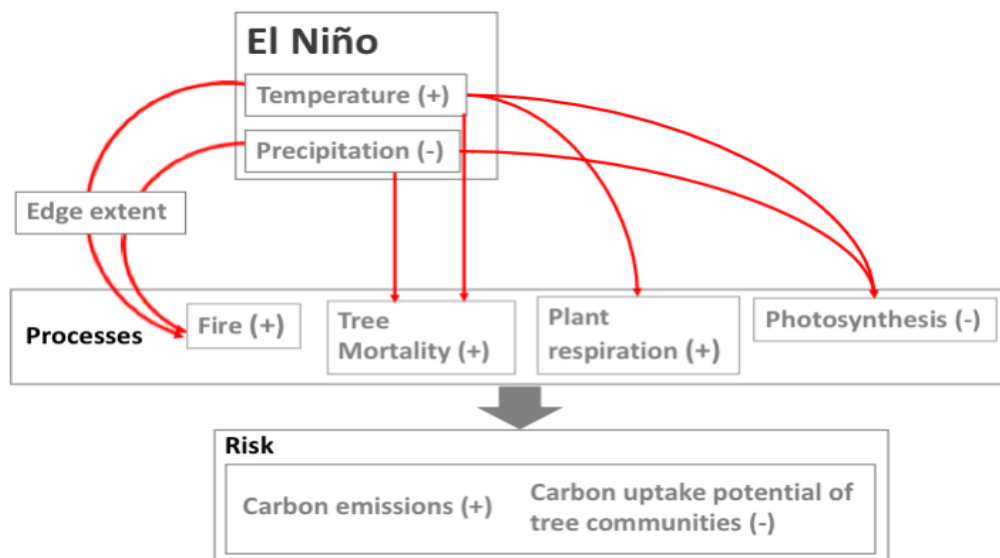


Figure S1. Expected impacts of El Niño events on ecological and physiological processes leading to alterations to the tropical forest carbon cycle. El Niño events are known to increase (+) temperature (T) and decrease (-) precipitation (P) within the tropical forest realm. These changes in climate have potential effects on a series of processes within the forest (red arrows). Greater T will increase soil and plant respiration, and photosynthetic rates may exceed their T threshold above which carbon assimilation decreases. The decrease in P combined with higher T will increase vapor pressure deficit (VPD) leading to closure of the stomata and reduction of photosynthesis. Lower P may decrease soil water, which in combination with higher VPD can lead to hydraulic failure of trees and potentially tree death [8]. Under drier and hotter conditions, the forest becomes more

flammable. The odds of fire are strongly related to forest fragmentation. Fragmented areas are more accessible by people, increasing the chance of human-driven ignition [9]. In addition, edge effects lead to a hotter and more arid microclimate, accentuating any El Niño-driven increases in T and decreases in P, also increasing the chances of fire. Combined, these processes are expected to lead to greater carbon emissions and reduced carbon uptake by tropical forest trees during El Niño years.

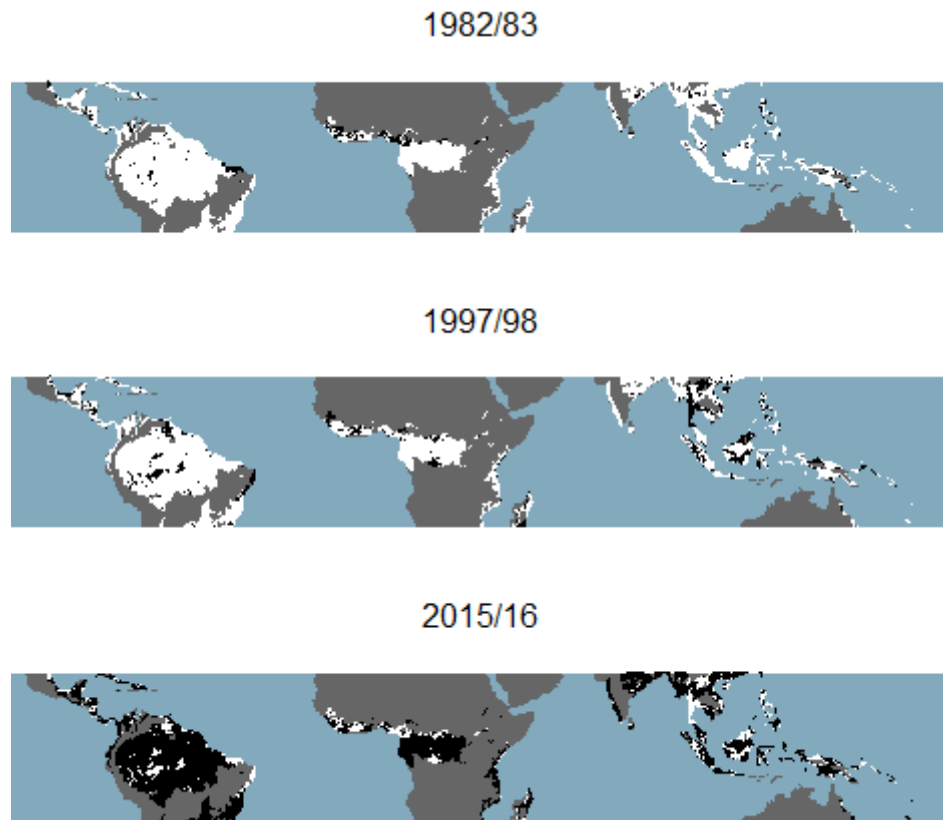


Figure S2. Occurrence of greatest risk in each grid cell across the three El Niños. Black indicates the El Niño in which grid cells had their highest risk score. Note: a grid cell can only be black in one El Niño.

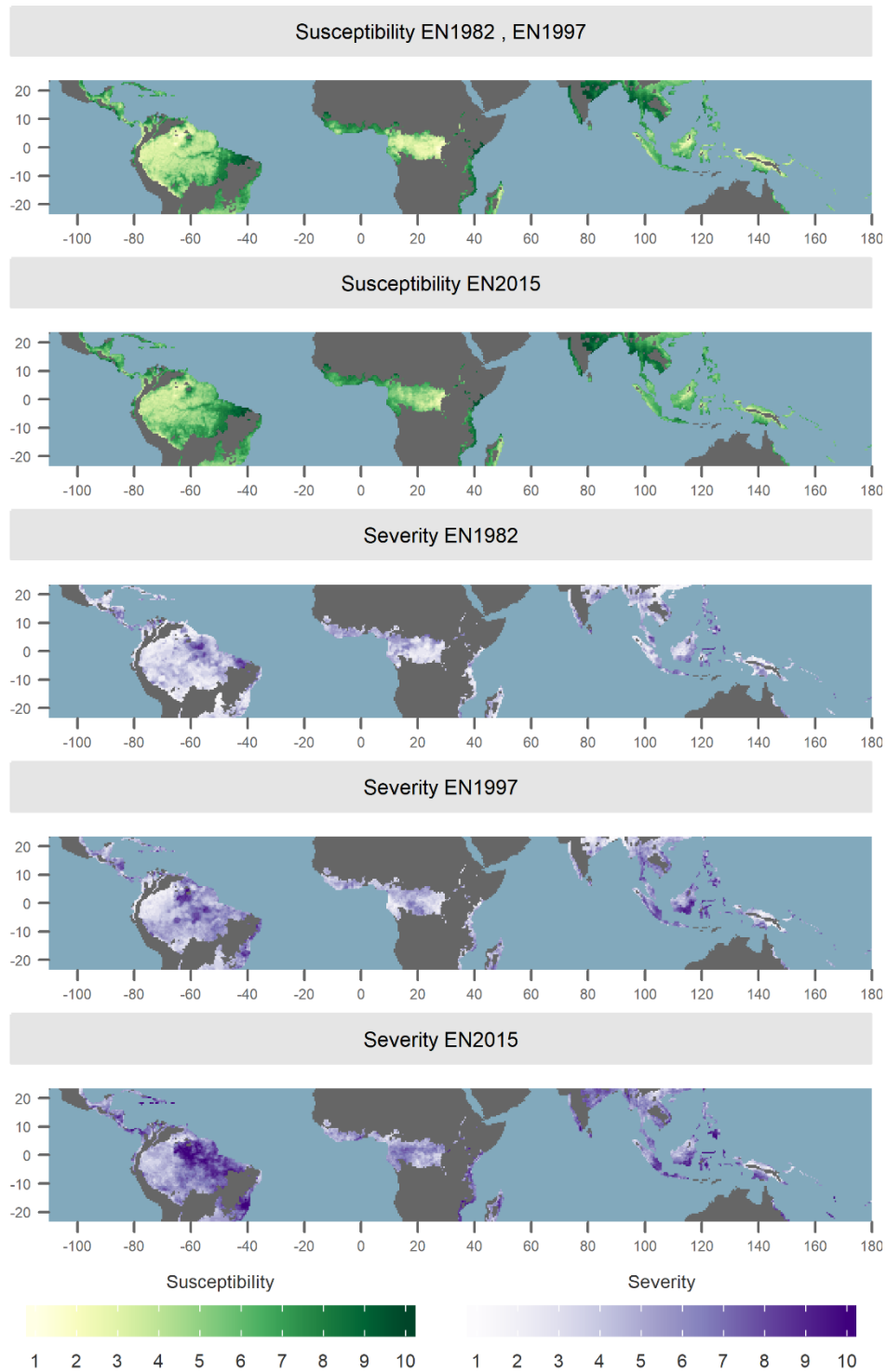


Figure S3. El Niño risk calculated from global susceptibility and mean-based severity. Top panel - El Niño1982 and El Niño1997 susceptibility using forest edge data from the year 2000. Second panel - El Niño 2015 susceptibility using forest edge data from 2014. Lower three panels - severity scores for El Niño 1982, El Niño 1997 and El Niño 2015. The x-axes represent longitude and y-axes latitude.

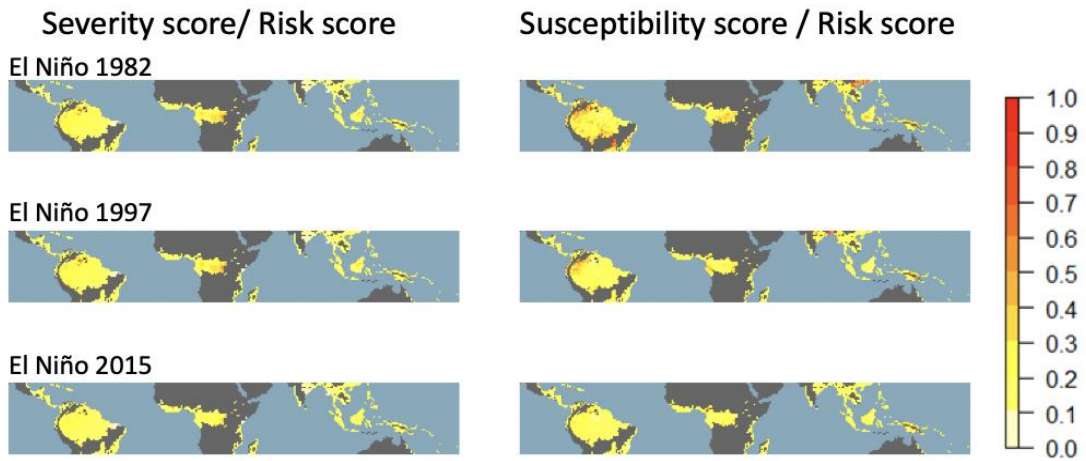


Figure S4. Proportion of risk score due to severity and susceptibility in each El Niño. Maps show severity or susceptibility scores divided by risk scores. Note that contributions are often small as the risk score was calculated by multiplying severity and susceptibility.

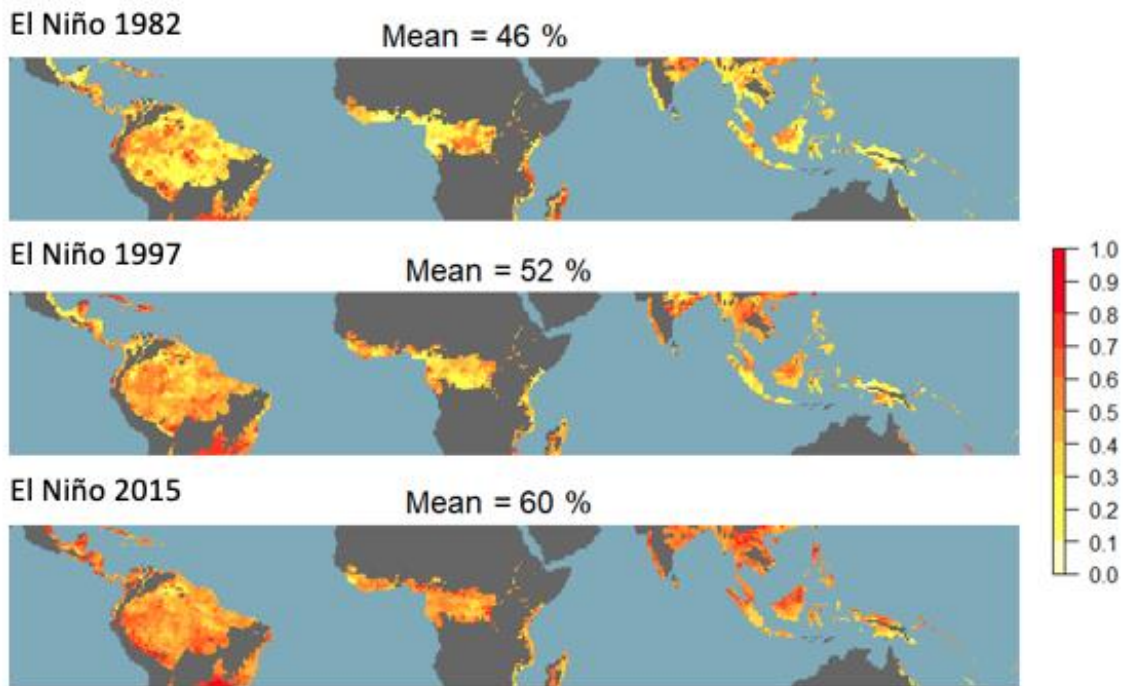


Figure S5. Proportion of severity score in each El Niño attributable to temperature. Red represents a greater proportion of the severity metric attributed to temperature. At the top of each graph we present the mean value across every cell for each El Niño. Remaining variation is due to MCWD.

score using Mann-Whitney tests ($P \leq 0.005$). The 2015 fire anomaly data for the Amazon basin was resampled to the resolution of our risk maps, then for each grid-cell in the Amazon Basin we extracted the fire anomaly and the susceptibility, severity and risk scores. This gave a data frame where each row has the fire anomaly, susceptibility score, severity score and risk score of a grid-cell. Relationships between fire anomaly and these scores were assessed using Kendall's rank correlation. We also converted the fire anomalies to binary variables indicating whether or not fire anomalies were greater than zero, and then tested if the susceptibility and other scores differed between binary fire categories.

References

1. Harris, I., P. D. Jones, T. J. Osborn, and D. H. Lister. "Updated High-Resolution Grids of Monthly Climatic Observations – the Cru Ts3.10 Dataset." *International Journal of Climatology* 34, no. 3 (2014): 623-42.
2. Schneider, U., A. Becker, P. Finger, A. Meyer-Christoffer, B. Rudolf, and M. Ziese. "Gpcc Full Data Reanalysis Version 7.0: Monthly Land-Surface Precipitation from Rain Gauges Built on Gts Based and Historic Data." Boulder, CO: Research Data Archive at the National Center for Atmospheric Research, Computational and Information Systems Laboratory, 2016.
3. Huffman, George J., David T. Bolvin, Eric J. Nelkin, David B. Wolff, Robert F. Adler, Guojun Gu, Yang Hong, Kenneth P. Bowman, and Erich F. Stocker. "The Trmm Multisatellite Precipitation Analysis (Tmpra): Quasi-Global, Multiyear, Combined-Sensor Precipitation Estimates at Fine Scales." *Journal of Hydrometeorology* 8, no. 1 (2007): 38-55.
4. Dee, D. P., S. M. Uppala, A. J. Simmons, P. Berrisford, P. Poli, S. Kobayashi, U. Andrae, M. A. Balmaseda, G. Balsamo, P. Bauer, P. Bechtold, A. C. M. Beljaars, L. van de Berg, J. Bidlot, N. Bormann, C. Delsol, R. Dragani, M. Fuentes, A. J. Geer, L. Haimberger, S. B. Healy, H. Hersbach, E. V. Hólm, L. Isaksen, P. Kållberg, M. Köhler, M. Matricardi, A. P. McNally, B. M. Monge-Sanz, J.-J. Morcrette, B.-K. Park, C. Peubey, P. de Rosnay, C. Tavolato, J.-N. Thépaut, and F. Vitart. "The Era-Interim Reanalysis: Configuration and Performance of the Data Assimilation System." *Quarterly Journal of the Royal Meteorological Society* 137, no. 656 (2011): 553-97.
5. Olson, David M., and Eric Dinerstein. "The Global 200: Priority Ecoregions for Global Conservation." *Annals of the Missouri Botanical Garden* 89, no. 2 (2002): 199-224.
6. Aragão, Luiz E. O. C., Y. Malhi, R. M. Roman-Cuesta, S. Saatchi, L. O. Anderson, and Y. E. Shimabukuro. "Spatial Patterns and Fire Response of Recent Amazonian Droughts." *Geophysical Research Letters* 34, no. 7 (2007): 1-5.
7. Hansen, M. C., P. V. Potapov, R. Moore, M. Hancher, S. A. Turubanova, A. Tyukavina, D. Thau, S. V. Stehman, S. J. Goetz, T. R. Loveland, A. Kommareddy, A. Egorov, L. Chini, C. O. Justice, and J. R. G. Townshend. "High-Resolution Global Maps of 21st-Century Forest Cover Change." *Science* 342, no. 6160 (2013): 850-53.
8. Rowland, Lucy, A. C. L. Da Costa, D. R. Galbraith, R. S. Oliveira, O. J. Binks, A. A. R. Oliveira, A. M. Pullen, C. E. Doughty, D. B. Metcalfe, S. S. Vasconcelos, L. V. Ferreira, Y. Malhi, J. Grace, M. Mencuccini, and P. Meir. "Death from Drought in Tropical Forests Is Triggered by Hydraulics Not Carbon Starvation." *Nature* 528 (2015): 119-22.
9. Alencar, Ane A., Paulo M. Brando, Gregory P. Asner, and Francis E. Putz. "Landscape Fragmentation, Severe Drought, and the New Amazon Forest Fire Regime." *Ecological Applications* 25, no. 6 (2015): 1493-505.